Available online at www.sciencedirect.com
ScienceDirect
Trans. Nonferrous Met. Soc. China 35(2025) 4038−4049
Transactions of Nonferrous Metals Society of China
www.tnmsc.cn

Role of Er on pore and microstructure of Al−Mg−Er−Zr weld joints produced by tandem GMAW

Jia-hui LI[1,2], Hai-chao CUI[1,2], Chen-dong SHAO[1,2], Ling LAN[1,2,3], Feng-gui LU[1,2]

1. Shanghai Key Laboratory of Materials Laser Processing and Modification, Shanghai Jiao Tong University, Shanghai 200240, China;
2. School of Materials Science and Engineering, Shanghai Jiao Tong University, Shanghai 200240, China;
3. Shanghai Shipbuilding Technology Research Institute, China Shipping Group Company, Shanghai 200032, China

Received 2 March 2024; accepted 5 August 2024

Abstract: A novel Al−Mg−Er−Zr alloy was welded by highly efficient tandem GMAW, and the effect of Er on the porosity, microstructure and mechanical properties of the weld joints were investigated by comparing them with Al5083 alloy weld joints. The results showed that compared to the welds without Er addition, the porosity decreased from 0.78% to 0.38%, which was attributed to the ability of Er to reduce the content of free hydrogen in the welds. Furthermore, the grain size near the fusion boundary and weld metal (WM) was significantly refined with the addition of Er. Grain refinement near the fusion boundary was attributed to the heterogeneous nucleation induced by $Al_3(Er,Zr)$ from base metal, while grain refinement in WM was caused by the hindering effect of Al_3Er on grain boundary migration. Additionally, the ultimate tensile strength of the weld joints increased from 272.44 to 338.74 MPa with Er addition. The precipitation strengthening induced by Al_3Er contributed to an increase by 20% in strength.

Key words: Al−Mg−Er−Zr alloy; tandem GMAW; pore; microstructure; mechanical properties

1 Introduction

Al−Mg alloys with high specific strength and good corrosion resistance have been widely used in aerospace, shipbuilding, and new energy vehicle fields [1−3]. As typical non-heat-treated strengthening alloys, Al−Mg alloys achieve strength through solution-strengthening and work-hardening of Mg solute atoms [4]. However, the content of Mg is typically restricted to 3−6 wt.% to reduce the formation of Al_3Mg_2, which is harmful for the corrosion and strength properties of Al−Mg alloys [5,6]. Considering this, adding other elements in Al−Mg alloys is necessary to acquire high mechanical performance.

Micro-alloying as an effective way has attracted considerable attention during the past several decades [7,8]. The alloying elements, such as transition elements (Ti, Zr, Mn, etc.) and rare earth elements (Sc, Er, etc.), can refine grain size and improve the strength properties of Al−Mg alloys [9−11]. Among them, Er, with active chemical properties and lower prices, has emerged as the most promising micro-alloying element for Al−Mg alloys [12]. Extensive research has claimed that a fine, coherent $L1_2$ structure Al_3Er with high thermal stability can form during Al−Er solid solution decomposition and can be amplified by the simultaneous addition of Zr to create $Al_3(Er,Zr)$ [13−15]. It has been reported that these precipitates can optimize the microstructure [16], hinder the grain

Corresponding author: Hai-chao CUI, Tel: +86-21-34202814, E-mail: haichaocui@sjtu.edu.cn;
Feng-gui LU, Tel: +86-21-34203024, E-mail: lfg119@sjtu.edu.cn
https://doi.org/10.1016/S1003-6326(25)66928-7

boundary [17], and pin the dislocation [18]. Consequently, a new type of Al−Mg−Er−Zr alloy with high thermal stability and superior mechanical properties was designed.

In order to make Al−Mg−Er−Zr alloy widely used in industrial production, researchers [19,20] have focused on the welding techniques for this alloy in recent years, including tungsten inert gas welding (TIG), laser beam welding [21], and friction stir welding (FSW) [22,23]. Although the above methods are suitable for welding Al−Mg−Er−Zr alloy with thin thickness, there are still lack of advanced welding methods for this kind of alloy as the thickness increases, which maintain good quality and efficiency. In addition to the welding method, the filler metal is also a key factor to be considered. Nowadays, the filler metal containing Er is regarded as the best choice for welding Al−Mg−Er−Zr alloy, in accordance with the principle of strength matching [24]. Therefore, the effect of Er on weld joints needs to be assessed. PENG et al [25] found that Er in the molten pool during selective laser melting decreased the porosity from 5.9% to 3.4%. YANG et al [26] and SUN et al [27] acutely observed that many refined equiaxed grains dominated near the fusion boundary of Al−Mg−Er−Zr alloy weld joints, contrary to the columnar grains in ordinary Al−Mg alloys. Moreover, the tensile strength and hardness of the weld joints were improved with the addition of Er, attributed to the effect of grain refinement strengthening and precipitation strengthening from $Al_3Er/Al_3(Er,Zr)$ [28−30]. These findings have revealed that adding Er in the welds effectively suppresses porosity and enhances strength. However, the mechanism by which Er affects weld porosity remains unclear, and the influence of Er on the mechanical properties of the weld joints has only been qualitatively discussed. Consequently, further fundamental research is required to clarify the role of Er on the weld porosity and to precisely determine its impact on the mechanical properties of weld joints.

In this study, a highly efficient tandem GMAW method was used to weld Al−Mg−Er−Zr alloy with 10 mm in thickness. Based on this, the mechanism of Er on porosity suppression was clarified by investigating the interaction between Er and hydrogen in the weld metal (WM). The effect of Er on the microstructure and strength properties of the weld joints was discussed and compared with the weld joints without Er. The results of this study provide a systematic insight into the role of Er on the porosity and microstructure of weld joints, providing theoretical support for the further application of Al−Mg−Er−Zr alloy in industrial production.

2 Experimental

The base metals (BMs) employed to manufacture weld joints were a new type of alloy named Al−Mg−Er−Zr and commercialized Al5083. Micro-alloying ER5E61 and normal ER1561 alloys, both with diameters of 1.2 mm, were selected as the filler metals (FMs) to weld Al−Mg−Er−Zr and Al5083 alloys, respectively. The chemical compositions of the BMs and FMs were determined by inductively coupled plasma atomic emission spectroscopy (ICP-AES), as listed in Table 1.

As shown in Fig. 1(a), Fronius TPS 5000 welding system was used to manufacture butt joints with V-type grooves, as shown in Fig. 1(c). The distance between the two wires along the welding direction was 10 mm, with the wire extension length being 18 mm. The two welding power sources worked in synergic pulse mode with a phase difference of 180°. The average welding current, voltage and speed were 187 A, 23.4 V and 360 mm/min respectively. The shielding gas was pure argon, and its flow rate was 25 L/min.

The specimens were prepared from the transverse section of the weld joints and mechanically polished, and then were etched with

Table 1 Chemical composition of BMs and FMs (wt.%)

Alloy	Cr	Cu	Fe	Mg	Mn	Si	Ti	Zn	Zr	Er	Al
Al−Mg−Er−Zr	0.01	0.01	0.09	6.12	0.87	0.01	0.03	0.01	0.10	0.11	Bal.
Al5083	0.09	0.05	0.12	4.51	0.66	0.11	0.01	0.03	−	−	Bal.
ER5E61	0.01	0.01	0.08	5.86	1.02	0.06	0.01	0.01	0.10	0.26	Bal.
ER1561	0.02	0.02	0.10	5.65	0.87	0.05	0.04	0.02	0.11	−	Bal.

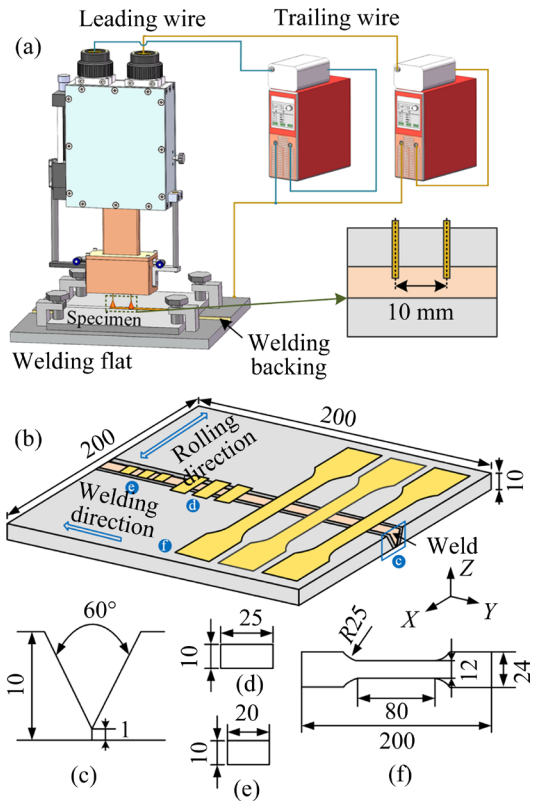

Fig. 1 Schematic of tandem GMAW system (a), location of specimens (b), shape and dimension of groove (c), metallographic specimen (d), X-ray specimen (e), and tensile specimen (f) (unit: mm)

Keller reagent (composed of 1 mL HF + 1.5 mL HCl + 2.5 mL HNO_3 + 95 mL deionized water) for 30 s. The specific dimensions of the specimens are shown in Fig. 1(d). The microstructure was then characterized using optical microscopy (OM, Zeiss Imager A2m), scanning electron microscopy (SEM, TESCAN GAIA3 and VEGA3) equipped with Time-of-Flight Secondary Ion Mass Spectrometry (TOF-SIMS) and electron back-scattered diffraction (EBSD) systems. EBSD samples were electro-polished with the electrolyte (5 ml $HClO_4$ + 95 mL CH_3CH_2OH) at the voltage of 30 V for 30 s. Channel 5 software was used to analyze the grain size, average misorientation, and crystallographic orientation. Thin foils for transmission electron microscopy (TEM, JEM−2100) testing were prepared by twin-jet polishing. Nano precipitates were observed using TEM equipped with selected area electron diffraction (SAED) at operating voltage of 200 kV. The composition of the precipitates was measured using TEM−EDS point scan mode. Quantitative analysis of the precipitates was conducted using Image-Pro software.

The 3D distribution of pores in the weld joints was detected by advanced X-ray microscopy (XRM, Zeiss Xradia 520), and the data were analyzed with Dragonfly software. The test parameters were operating voltage of 140 kV, operating power of 10 W, exposure time of 1 s and a resolution of 21.989 μm. Vickers microhardness across the Al−Mg−Er−Zr weld joints and Al5083 weld joints were tested using a load of ~2.9 N and a holding time of 10 s. Tensile tests were performed on a universal testing machine (Z100 TEW) with displacement rate of 1 mm/min at room temperature (25 °C) in accordance with the GB/T 2651−2008 and GB/T 228.1−2010. The standard tensile specimens are shown in Fig. 1(f).

3 Results and discussion

3.1 Effect of Er on hydrogen pores

Figures 2(a) and (b) show the 3D morphology and distribution of pores in the WM with and without Er addition, respectively. According to the diameters of pores and the limitations of XRM resolution, the pores in the WM can be divided into three categories: 50−100 μm, 100−200 μm and over 200 μm, as shown in Figs. 3(a) and (b). Among these the categories, the fraction of 50−100 μm in diameter accounted for 74.72% and 60.65% for the WM with and without Er addition, which indicated that both weld joints were characterized with mainly small sized pores. With the addition of Er, the porosity was reduced from 0.78% to 0.38%. The maximum size of the pores decreased from 380 to 260 μm, and the fraction of pores over 200 μm decreased from 8.61% to 2.43%. The above results showed that the addition of Er decreased the size of pores in the WM and reduced the welding porosity.

It was believed that the formation of hydrogen pores is mainly due to the different solubilities of hydrogen in molten and solid aluminum [31], which provided large amount of free hydrogen in the weld during solidification process. Notably, Er in the weld decreased the content of free hydrogen by trapping it or reacting with it, as shown in Fig. 4. According to Hume−Rothery theory, the solid solubility of Er in α-Al is extremely low, and its limited solubility in the equilibrium state is only 0.05 wt.% [30]. Therefore, a large number of Er-rich precipitates sized 1−2 μm with different morphologies, formed during the

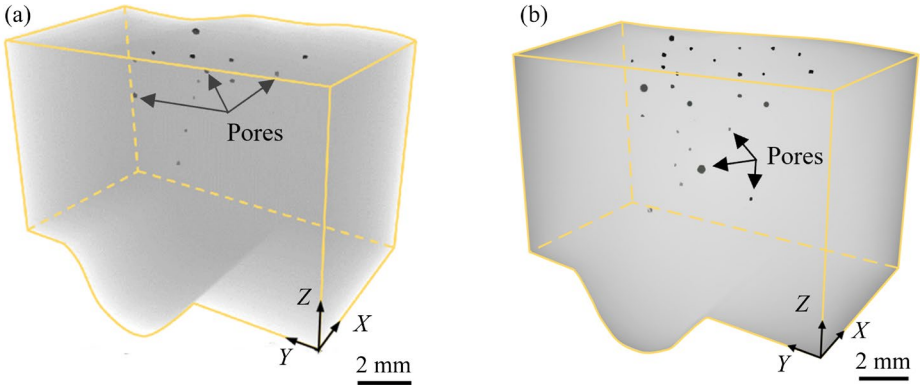

Fig. 2 3D characteristics of pores in WM of Al alloy with and without Er: (a) Al−Mg−Er−Zr alloy; (b) Al5083 alloy

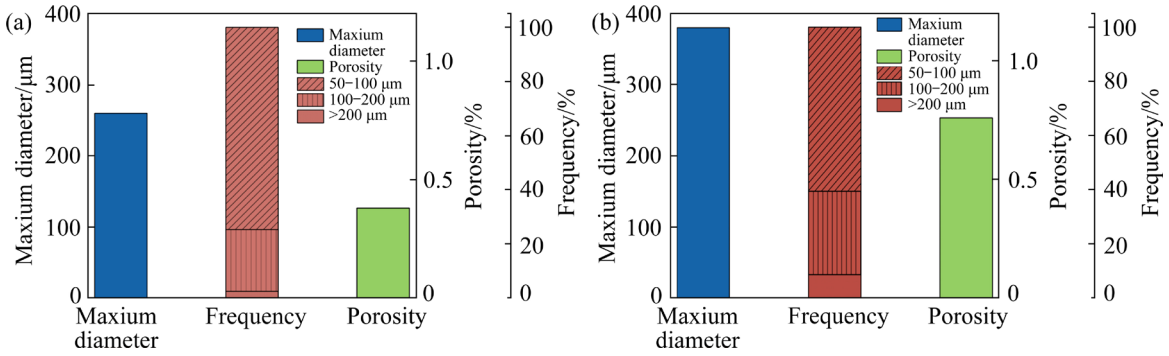

Fig. 3 Statistical results of pores in WM of Al alloy with and without Er: (a) Al−Mg−Er−Zr alloy; (b) Al5083 alloy

solidification process, as shown in Fig. 4(a). Figures 4(b−d) clearly demonstrate that these Er-enriched precipitates trapped many hydrogens in the weld. These trapped hydrogens could not nucleate and grow into bubbles, and therefore had no effect on the porosity. Moreover, some ErH clusters were observed near these precipitates, as shown in Fig. 4(e). HAN et al [32] pointed out that lanthanides could react with free hydrogen in the melt to generate ReH_2. Er and hydrogen in the molten pool would react as follows:

$$Er+2[H]\rightarrow ErH_2 \quad (1)$$

From the thermodynamic point of view, the conditions for the above reaction that occurred spontaneously are as follows [33]:

$$\Delta G=\Delta H^{\Theta}-T\Delta S^{\Theta}=-220900+147.8T<0 \quad (2)$$

where ΔG is Gibbs free energy, ΔH^{Θ} and ΔS^{Θ} are respectively standard molar enthalpy (J/mol) and entropy (J/(mol·K)) of the Er−H system, and T is the temperature in K.

When the temperature is lower than 1494.6 K, the reaction between Er and hydrogen is spontaneous with decreased Gibbs free energy. Therefore, Er continuously reacted with hydrogen to form ErH_2 during the solidification of the molten pool. The ErH clusters (generated by ErH_2 ionization) near the Er-enriched precipitates further proved the above process, indicating that Er could also reduce the content of free hydrogen by forming hydrides.

Figure 5 schematically displays the effect of Er on weld porosity. As shown in Fig. 5(a), plenty of dispersed Er-enriched precipitates and oxides formed in the molten pool during solidification. With the decrease in temperature, large amounts of hydrogen were released from the melt and attracted by these precipitates, as shown in Fig. 5(b). Due to the Er-enriched precipitates acting as hydrogen trapping sites and forming hydrides, the amount of hydrogen bubbles was reduced significantly, as shown in Fig. 5(c).

3.2 Effect of Er on grain refinement

The microstructure of weld joints without and with the addition of Er is presented in Fig. 6. The

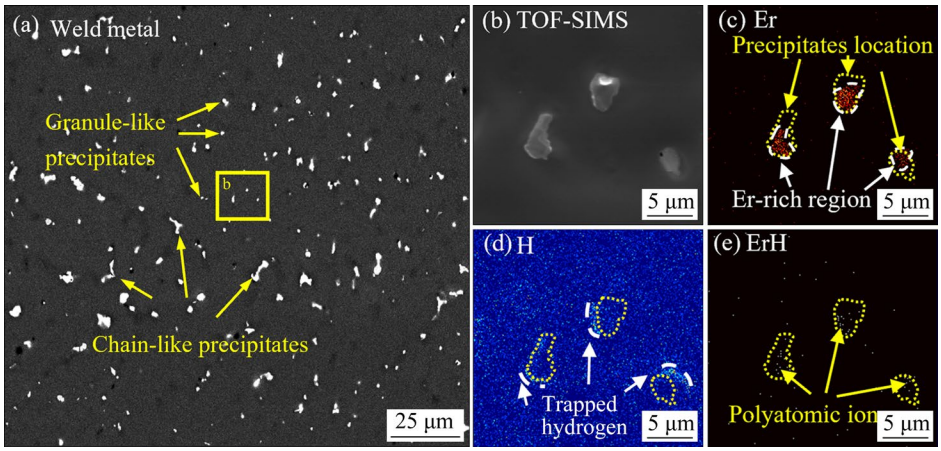

Fig. 4 (a) Distribution and morphology of precipitates in weld metal; (b) TOF-SIMS scanning region; (c–e) TOF-SIMS scanning results highlighting Er, H, and polyatomic ion ErH, respectively

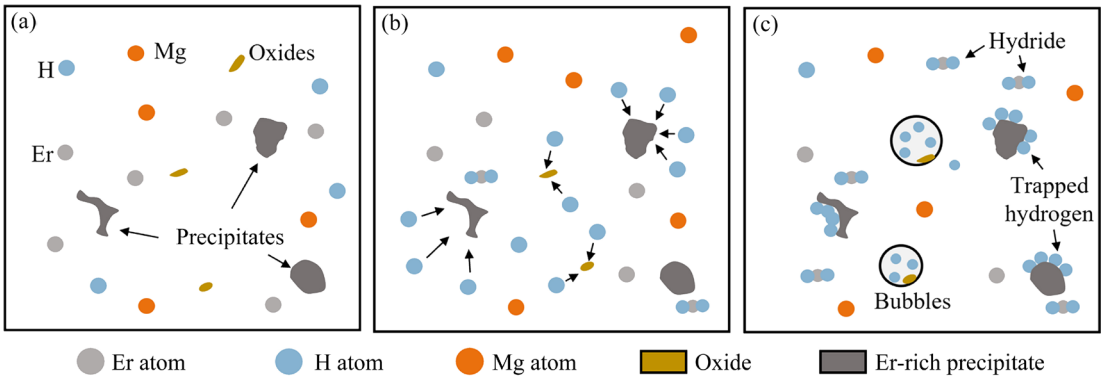

Fig. 5 Schematic diagram of effect of Er on weld porosity: (a) Formation of Er-rich precipitate; (b) Release of hydrogen; (c) Effect of Er on hydrogen

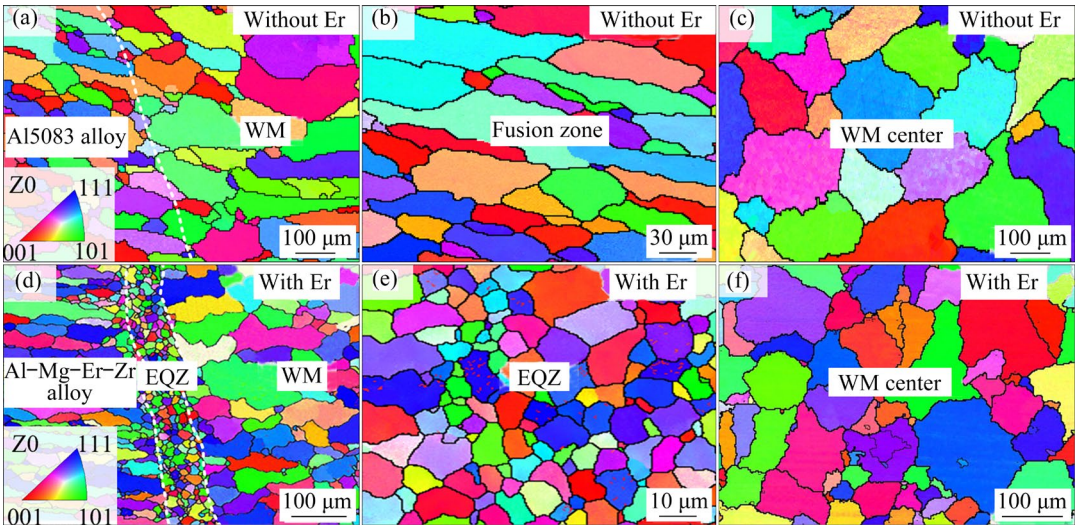

Fig. 6 IPF maps of weld joints with and without Er: (a, b, c) Al5083 alloy; (d, e, f) Al−Mg−Er−Zr alloy

fusion zone of Al5083 weld joints was composed of typical columnar grains with obvious epitaxial growth orientation, as shown in Fig. 6(b), which was consistent with the higher temperature gradient (G) and lower crystal growth rate (R) near the boundary of the molten pool. However, with the addition of Er, a narrow band of equiaxed grain zone (EQZ) appeared along the fusion boundary, as shown in

Fig. 6(d). The width of the EQZ was about 60 μm. It was noted that grains in this region were significantly refined and had no orientation relationship with each other (Fig. 6(e)). The average diameter of grains in EQZ was 8.87 μm.

The microstructures of the WM center without and with Er are shown in Figs. 6(c) and (f). The maps illustrated that coarsen equiaxed grains appeared in the WM center in both cases, which agreed with the decrease in the G/R ratio from the boundary to the center. However, the average diameters of grains at the center of WM with and without Er were 53.79 and 86.96 μm, respectively, showing that the addition of Er reduced the grain size at the WM center significantly.

The TEM image (Fig. 7(a)) taken from EQZ showed that the heterogeneous nucleation particle was found within equiaxed grains. The SAED result revealed that the particle has $L1_2$ superlattice structure, as demonstrated in Fig. 7(b). Combined with the EDS results, it could be inferred that the particle was $Al_3(Er,Zr)$, which evolved from Al_3Er. The lattice constant of this particle was close to that of the matrix Al, as shown in Fig. 7(e). The mismatch between the particle and the matrix was 0.16 belonging to the semi-coherent interface, which implied that this kind of particles could act as the effective site for heterogeneous nucleation, promoting the formation of equiaxed grains. It was believed that the Al_3Er or $Al_3(Er,Zr)$ particles in BM were the essential sources of heterogeneous nucleation particles for EQZ. One reason was that these particles with the melting point of 1070 °C [34] would not completely melt at the molten pool boundary, which was approximately 900 °C [35]). Moreover, the size of these unmelted particles was similar to that of the particles in BM as compared in Figs. 7(a) and (f), further proving that the particles in EQZ originated from BM. Due to the existence of these unmelted particles, the growth of grains at the molten pool boundary could overcome the high G/R ratio to form equiaxed grains.

The grain refinement in WM center could be explained by the theory of grain growth, where the grain size was controlled by grain boundary migration. It could be found from Fig. 8(a) that several fine particles distributed along the grain boundary in Al−Mg−Er−Zr weld joints, which could hinder the grain boundary migration during grain growth. There were two kinds of particles at the grain boundary, as shown in Fig. 8(b). Based on the SAED and EDS results, the coarsening particles were considered as Al_3Zr, while the fine particles were inferred to be Al_3Er enriched with Mg atoms. The resistance of grain boundary migration could be explained by the Zener's formula [36]:

$$P_Z=\frac{3}{4}\gamma\frac{f}{r} \tag{3}$$

where P_Z is the Zener force representing the resistance of particles to grain boundaries, γ is the migration energy, f is the volume fraction of particles, and r is the radius of particles.

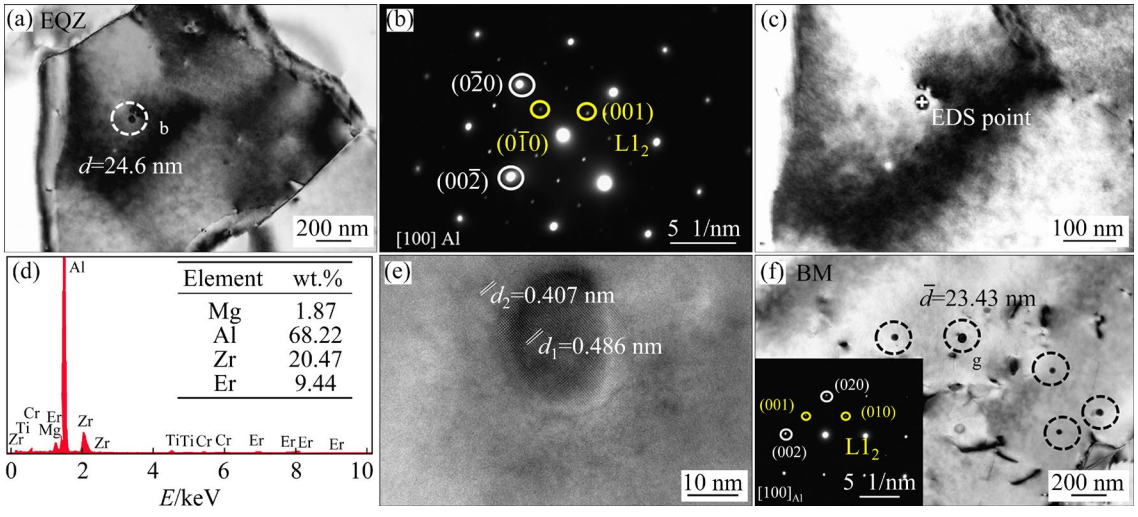

Fig. 7 TEM images taken from EQZ: (a) Heterogenous nucleation particle; (b) SAED pattern along [100] zone axis taken from (a); (c, d) TEM−EDS point scan region and results; (e) High-resolution image of particle; (f) Particles and SAED pattern in BM

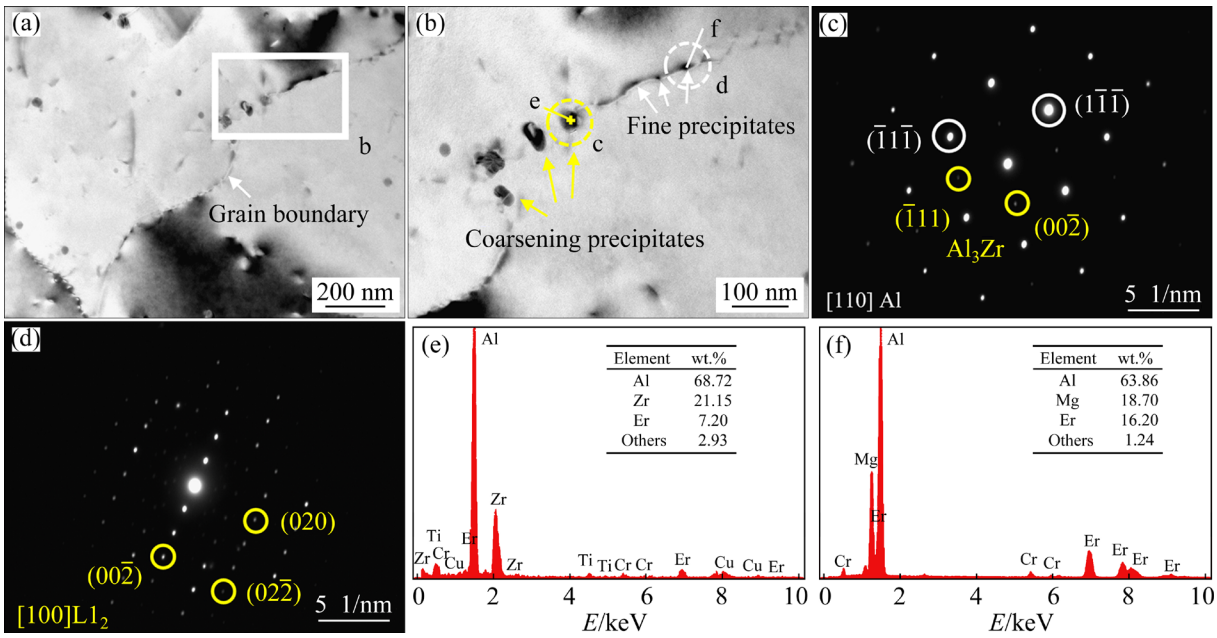

Fig. 8 (a) TEM image taken from Al−Mg−Er−Zr WM center; (b) Enlarged image highlighted by white square in (a); (c, e) SAED and EDS results of yellow dotted region in (b), respectively; (d, f) SAED and EDS results of white dotted region in (b), respectively

From Eq. (3), the particles with larger volume fractions and smaller sizes could provide greater resistance to grain boundaries migration. According to Al−Zr and Al−Er phase diagrams, the distribution coefficient (K) of Zr and Er in aluminum was opposite [30]. Specifically, K_{Zr}>1, whereas K_{Er}<1. Therefore, Er aggregated with higher concentration ahead of the solid−liquid interface than Zr during the solidification process, which more easily reached the eutectic composition to form plenty of Al_3Er. What's more, the Al_3Er particles with $L1_2$ superlattice structure had lower lattice mismatch with the aluminum matrix compared to Al_3Zr, making the coarsening rate of Al_3Er slower than Al_3Zr. Therefore, the Al_3Er particles, along the grain boundary in the form of small size and large quantities, played a dominant role in inhibiting grain growth.

3.3 Mechanical properties of weld joints

Figure 9 shows the microhardness distribution across the weld joints. The microhardness testing of the BMs showed that the Al−Mg−Er−Zr alloy had an average microhardness of HV 91, which was much higher than Al5083 alloy (HV 76). Under the welding thermal cycle, the softening phenomenon occurred in both weld joints, resulting in the heat-affected zone (HAZ). The width of HAZ in

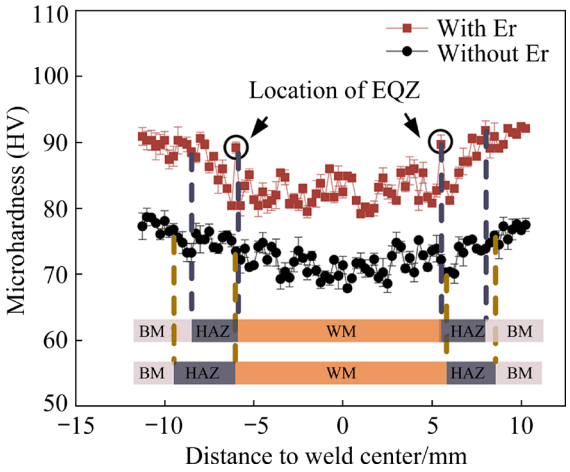

Fig. 9 Microhardness distribution of weld joints with and without Er

Al−Mg−Er−Zr alloy was narrower than that in Al5083 alloy, which proved that the thermal stability of Al−Mg alloys was improved with the addition of Er. It was worth noting that the EQZ in Al−Mg−Er−Zr alloy had a relatively high microhardness of HV 89, which was contrary to the lowest microhardness of EQZ in welded 7xxx aluminum alloys [37]. Moreover, the micro-hardness of the WM was approximately HV 71 without Er and HV 83 with Er. This indicated that the existence of Er improved the microhardness of the WM greatly.

The tensile stress−strain curves of the weld joints are shown in Fig. 10. Both weld joints exhibited serrated curve during tensile process, which was attributed to the dynamic strain aging caused by the dynamic interaction of diffusing solutes and mobile dislocations [38]. The weld joints with the addition of Er exhibited the ultimate tensile strength (UTS) of 338.74 MPa and elongation (EI) of 9.68%, whereas the weld joints without the addition of Er exhibited the UTS of 272.44 MPa and EI of 8.08%. It can also be seen that both weld joints fractured within WM. The tensile properties of the weld joints represented the properties of WM in both cases, which proved that the addition of Er improved the tensile properties of WM. Moreover, the fracture surfaces of both weld joints were characterized by shallow dimples, as shown in Fig. 11, consistent with the tensile properties testing results. However, a few deformed pores were found in the WM without the addition of Er, which reduced the bearing area and decreased the tensile properties of the weld joints to some degree.

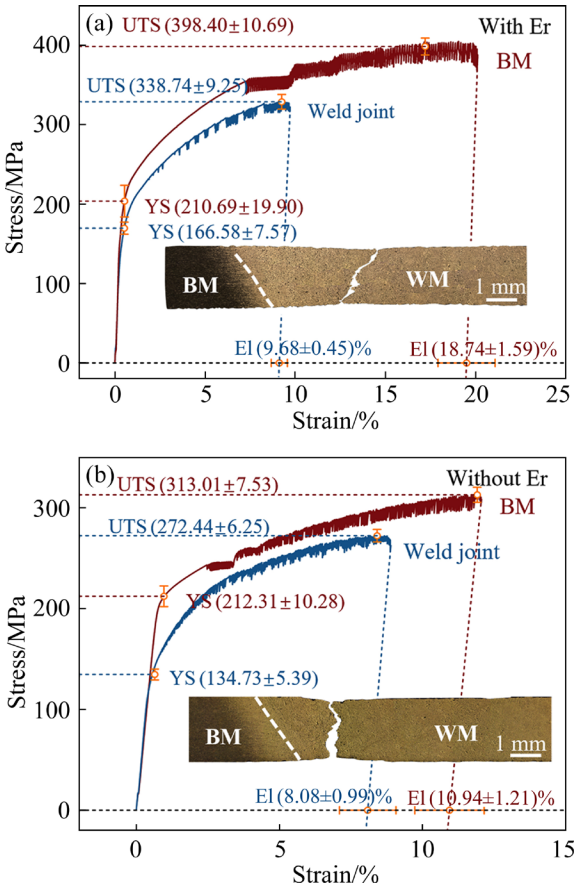

Fig. 10 Stress−strain curves of weld joints with and without Er: (a) Al−Mg−Er−Zr alloy; (b) Al5083 alloy

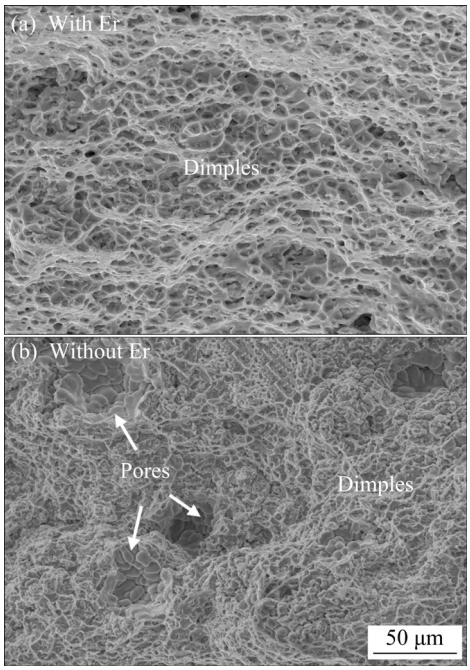

Fig. 11 Fracture surface of weld joints with and without Er: (a) Al−Mg−Er−Zr alloy; (b) Al5083 alloy

To understand the mechanism of strength improvement with the addition of Er, the classic analytical models of material strength were used in this study. Conventionally, the strength of materials could be estimated by calculating the contribution of grain size strengthening ($\Delta\sigma_{gb}$), dislocation strengthening ($\Delta\sigma_{dis}$), solid solution strengthening ($\Delta\sigma_{ss}$) and precipitation strengthening ($\Delta\sigma_{ppt}$). With the addition of Er, the grain size in WM was refined from 86.96 to 53.79 μm, and the dislocation density increased from 1.2×10^{13} to 2.5×10^{13} m^{-2}, as shown in Fig. 12. These refinement and density increase were caused by Al_3Er/$Al_3(Er,Zr)$ particles, inhibiting the migration of grain boundary and dislocation. Based on calculation using the Hall−Petch and Bailey−Hirsch equations (Eqs. (4) and (5)) [39], the contribution of $\Delta\sigma_{gb}$ and $\Delta\sigma_{dis}$ increased by 4.07 MPa and 5.67 MPa, respectively.

$$\Delta\sigma_{gb}=\sigma_0+Kd^{-1/2} \tag{4}$$

where σ_0 is the lattice resistance (σ_0=0 for aluminum alloy), K is the strength coefficient (K=0.14 for aluminum alloy), and d is the diameter of grains.

$$\Delta\sigma_{dis}=\alpha bG\sqrt{\rho} \tag{5}$$

where α is the material constant (α=0.5 for aluminum alloy), b is the magnitude of Burgers vector (b=0.284 nm for aluminum alloy), G is the shear

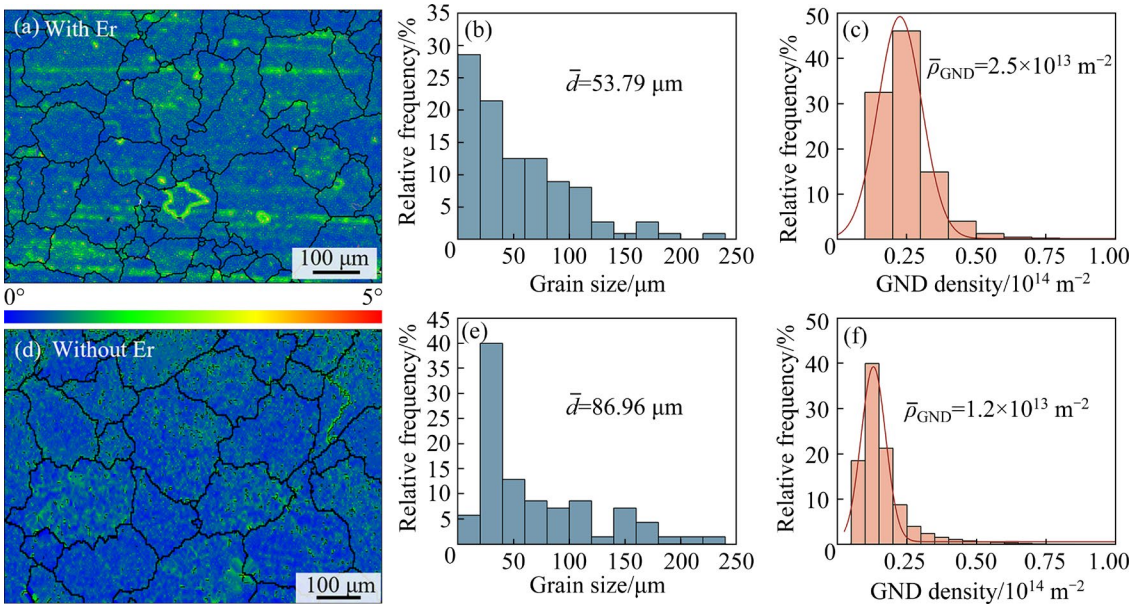

Fig. 12 GND maps (a, d), grain diameter distribution (b, e), and GND density (c, f) of WM with (a, b, c) and without (d, e, f) Er

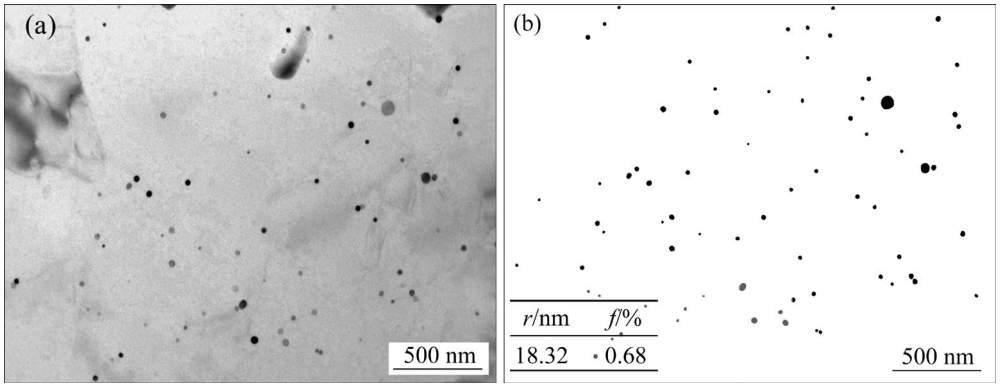

Fig. 13 TEM image taken from WM of Al−Mg−Er−Zr alloy weld joints (a), and binary processing results (b)

modulus (G=26 GPa for aluminum alloy), and ρ is the dislocation density.

Additionally, the contribution of $\Delta\sigma_{ppt}$ in Al−Mg weld joints without Er was usually ignored. However, due to the existence of Al_3Er/Al_3(Er,Zr) particles formed by the addition of Er in WM (see Fig. 13(a)), $\Delta\sigma_{ppt}$ could not be ignored any more. Given that these particles had a semi-coherent relationship with the matrix, dislocations could only bypass these particles. According to the Orowan bypassing mechanism, the effect of these particles on strength improvement could be expressed as follows [39]:

$$\Delta\sigma_{ppt}=\frac{0.4MGb}{\pi\sqrt{1-\nu}}\frac{\ln\left(\frac{2\bar{r}}{b}\right)}{L_p} \tag{6}$$

where M is the Taylor factor (M = 3.06 for aluminum alloy [36]), ν is the Poisson's ratio (ν =0.33 for aluminum alloy [36]), $\bar{r}=\sqrt{2/3}r$ in which r is the mean precipitates radius, and $L_p=2\bar{r}(\sqrt{\pi/(4f)}-1)$ in which f is the volume fraction of precipitates.

By binary processing, both r and f of these particles were extracted from the TEM image, as shown in Fig. 13(b). Taking these values into the above equation, the contribution of $\Delta\sigma_{ppt}$ with the addition of Er was calculated to be 56.13 MPa, which was the main reason for the strength improvement.

4 Conclusions

(1) With the addition of Er, a large number of Er-enriched precipitates were proved to be effective

hydrogen trapping sites, and ErH clusters generated by ErH_2 ionization formed in the weld. Due to the effect of Er on reducing hydrogen content, the maximum size of the pores decreased from 380 to 260 μm and the porosity of the weld joints decreased from 0.78% to 0.38%.

(2) The addition of Er refined the grains near the fusion boundary and WM center significantly. The EQZ near the fusion boundary formed with grain size around 8.87 μm since the Al_3Er or $Al_3(Er,Zr)$ particles in BM acted as heterogeneous nucleation sites. In the weld center, quantity of Al_3Er with nano size along the grain boundary hindered the grain growth, reducing the grain size from 86.96 to 53.79 μm.

(3) The microhardness and tensile properties of the weld joints improved with the addition of Er. The UTS of the weld joints increased from 272.44 to 338.74 MPa, in that the contribution of precipitate strengthening induced by Al_3Er accounting for an increase of 56.13 MPa.

CRediT authorship contribution statement

Jia-hui LI: Conceptualization, Formal analysis, Investigation, Data curation, Writing − Original draft; **Hai-chao CUI:** Formal analysis, Methodology, Validation; **Chen-dong SHAO:** Methodology, Resources, Software; **Ling LAN:** Resources, Funding acquisition; **Feng-gui LU:** Conceptualization, Supervision, Funding acquisition, Writing − Review & editing.

Declaration of competing interest

The authors declare that they have no known competing financial interests or personal relationships that could have appeared to influence the work reported in this paper.

Acknowledgments

The authors gratefully acknowledge the financial support by the National Key R&D Program of China (No. 2023YFB3407800), the National Natural Science Foundation of China (No. U2141213), and the experimental supports by Instrumental Analysis Center of Shanghai Jiao Tong University, China.

References

[1] WANG Yu, YANG Bo-wei, GAO Min-qiang, ZHAO Er-tuan, GUAN Ren-guo. Microstructure evolution, mechanical property response and strengthening mechanism induced by compositional effects in Al−6Mg alloys [J]. Materials & Design, 2022, 220: 110849.

[2] GUNGOR B, KALUC E, TABAN E, SIK A. Mechanical, fatigue and microstructural properties of friction stir welded 5083-H111 and 6082-T651 aluminum alloys [J]. Materials & Design, 2014, 56: 84−90.

[3] CLAUSEN A H, BØRVIK T, HOPPERSTAD O S, BENALLAL A. Flow and fracture characteristics of aluminum alloy AA5083-H116 as function of strain rate, temperature and triaxiality [J]. Materials Science and Engineering: A, 2004, 364: 260−272.

[4] RYEN Ø, HOLMEDAL B, NIJS O, NES E, SJŐLANDER E, EKSTRÖM H E. Strengthening mechanisms in solid solution aluminum alloys [J]. Metallurgical and Materials Transactions A, 2006, 37: 1999−2006.

[5] PAN Shi-wei, WANG Zi-dong, LI Chu-nan, WAN Di, CHEN Xiao-hua, CHEN Kai-xuan, LI Yan-jun. Achieving superior dispersion-strengthening effect in an AA5xxx Al−Mg−Mn alloy by mico-alloying [J]. Materials & Design, 2023, 226: 111647.

[6] ALGENDY A Y, LIU K, CHEN X G. Formation of intermetallic phases during solidification in Al−Mg−Mn 5xxx alloys with various Mg levels [J]. MATEC Web of Conferences, 2020, 326: 02002.

[7] LÜ Yi-zhen, WANG Qu-dong, ZENG Xiao-qin, DING Wen-jiang, ZHAI Chun-quan, ZHU Yan-ping. Effects of rare earths on the microstructure, properties and fracture behavior of Mg−Al alloys [J]. Materials Science and Engineering: A, 2000, 278: 66−76.

[8] ALGENDY A Y, LIU Kun, CHEN X G. Evolution of dispersoids during multistep heat treatments and their effect on rolling performance in an Al−5%Mg−0.8%Mn alloy [J]. Materials Characterization, 2021, 181: 111487.

[9] MIKHAYLOVSKAYA A V, PORTNOY V K, MOCHUGOVSKIY A G, ZADOROZHNYY M Y, TABACHKOVA N Y, GOLOVIN I S. Effect of homogenisation treatment on precipitation, recrystallisation and properties of Al−3%Mg−TM alloys (TM = Mn, Cr, Zr) [J]. Materials & Design, 2016, 109: 197−208.

[10] BAKARE F, SCHIEREN L, ROUXEL B, JIANG L, LANGAN T, KUPKE A, WEISS M, DORIN T. The impact of L12 dispersoids and strain rate on the Portevin-Le-Chatelier effect and mechanical properties of Al−Mg alloys [J]. Materials Science and Engineering: A, 2021, 811: 141040.

[11] XIAO Quan-feng, HUANG Ji-wu, JIANG Ying-ge, JIANG Fu-qin, WU Yun-feng, XU Guo-fu. Effects of minor Sc and Zr additions on mechanical properties and microstructure evolution of Al−Zn−Mg−Cu alloys [J]. Transactions of Nonferrous Metals Society of China, 2020, 30(6): 1429−1438.

[12] NIE Zuo-ren, WEN Sheng-pin, HUANG Hui, LI Bo-long, ZUO Tie-yong. Research progress of Er-containing aluminum alloy [J]. The Chinese Journal of Nonferrous Metals, 2011, 21: 2361−2370. (in Chinese)

[13] WEN S P, XING Z B, HUANG H, LI B L, WANG W, NIE Z R. The effect of erbium on the microstructure and mechanical properties of Al−Mg−Mn−Zr alloy [J]. Materials Science and Engineering: A, 2009, 516: 42−49.

[14] WEN S P, GAO K Y, LI Y, HUANG H, NIE Z R. Synergetic effect of Er and Zr on the precipitation hardening of Al−Er−Zr alloy [J]. Scripta Materialia, 2011, 65: 592−595.

[15] WU H, WEN S P, HUANG H, WU X L, GAO K Y, WANG W, NIE Z R. Hot deformation behavior and constitutive equation of a new type Al−Zn−Mg−Er−Zr alloy during isothermal compression [J]. Materials Science and Engineering: A, 2016, 651: 415−424.

[16] YANG Fu-bao, LIU En-ke, XU Jun, SHI Li-kai. Effect of Er on the microstructures and mechanical properties of as-cast Al−Mg−Mn−Zn−Sc−Zr−(Ti) filler metals [J]. Acta Metallurgica Sinica, 2008, 44: 911−916. (in Chinese)

[17] WEN S P, GAO K Y, HUANG H, WANG W, NIE Z R. Precipitation evolution in Al−Er−Zr alloys during aging at elevated temperature [J]. Journal of Alloys and Compounds, 2013, 574: 92−97.

[18] MOCHUGOVSKIY A G, MIKHAYLOVSKAYA A V, TABACHKOVA N Y, PORTNOY V K. The mechanism of $L1_2$ phase precipitation, microstructure and tensile properties of Al−Mg−Er−Zr alloy [J]. Materials Science and Engineering: A, 2019, 744: 195−205.

[19] YANG Dong-xia, LI Xiao-yan, HE Ding-yong, NIE Zuo-ren, HUANG Hui. Microstructural and mechanical property characterization of Er modified Al−Mg−Mn alloy tungsten inert gas welds [J]. Materials & Design, 2012, 34: 655−659.

[20] GAO Qing-wei, SHU Feng-yuan, HE Peng, DU Wen-bo. Microstructure and impact mechanical properties of multi-layer and multi-pass TIG welded joints of Al−Zn−Mg alloy plates [J]. Transactions of Nonferrous Metals Society of China, 2019, 29(12): 2496−2505.

[21] YANG Dong-xia, LI Xiao-yan, HE Ding-yong, HUANG Hui, ZHANG Li-ang. Study on microstructure and mechanical properties of Al−Mg−Mn−Er alloy joints welded by TIG and laser beam [J]. Materials & Design, 2012, 40: 117−123.

[22] LI Qi-lei, HUANG Guang-jie, CAO Yu, ZHANG Cheng-hang, HE Jie, JIANG Hao-nan, LIN lin, LIU Qing. Microstructure refinement, strengthening and ductilization mechanisms in Al−Mg−Mn−Er−Zr alloy with high Mn content by friction stir processing [J]. Materials Characterization, 2022, 189: 111939.

[23] JIANG Jing-yu, JIANG Feng, ZHANG Meng-han. Microstructure evolution and mechanical properties of Al−Mg−Sc−Zr alloy sheet after friction stir welding [J]. Transactions of Nonferrous Metals Society of China, 2023, 33: 1687−1700.

[24] FU Le, PENG Yong-yi, HUANG Ji-wu, DENG Ying, YIN Zhi-min. Microstructures and mechanical properties of gas tungsten arc welded joints of new Al−Mg−Sc and Al−Mg−Er alloy plates [J]. Materials Science and Engineering: A, 2015, 620: 149−154.

[25] PENG Zhi-bo, CUI Li, HE Ding-yong, GUO Xing-ye, ZENG Yong, CAO Qing, HUANG Hui. Effect of Er and Zr addition on laser weldability of AlSi10Mg alloys fabricated by selective laser melting [J]. Materials Characterization, 2022, 190: 112070.

[26] YANG Dong-xia, LI Xiao-yan, HE Ding-yong, HUANG Hui. Effect of minor Er and Zr on microstructure and mechanical properties of Al−Mg−Mn alloy (5083) welded joints [J]. Materials Science and Engineering: A, 2013, 561: 226−231.

[27] SUN Yi-wei, WANG Jia-long, SHI Yun, FEI Qin-nan, ZHAO Ning-shuang, NI Chao, WU Ji-li, DONG Yin-sheng, DAI Ting, DING Hui, HAO Meng-long. An SLM-processed Er- and Zr- modified Al−Mg alloy: Microstructure and mechanical properties at room and elevated temperatures [J] Materials Science and Engineering: A, 2023, 883: 145485.

[28] WEI Xiao-yuan, HUANG Hui, CHEN Zi-yong, WANG Wei, LI Cong-ying, NIE Zuo-ren. Microstructure and mechanical properties of Al−Mg−Mn−Zr−Er weld joints filled with Al−Mg−Mn−Zr and Al−Mg−Mn−Zr−Er weld wires [J]. Journal of Rare Earths, 2010, 28: 627−630.

[29] ZHAO Yan-qiu, ZHOU Xu-dong, LIU Ting, KANG Yue, ZHAN Xiao-hong. Investigate on the porosity morphology and formation mechanism in laser-MIG hybrid welded joint for 5A06 aluminum alloy with Y-shaped groove [J]. Journal of Manufacturing Processes, 2020, 57: 847−856.

[30] GUO Yan-wu, WEI Wu, SHI wei, ZHANG Bo, ZHOU Xiao-rong, WEN Sheng-ping, WU Xiao-lan, GAO Kun-yuan, RONG Li, HUANG Hui, NIE Zuo-ren. Effect of Er and Zr additions and aging treatment on grain refinement of aluminum alloy fabricated by laser powder bed fusion [J]. Journal of Alloys and Compounds, 2022, 912: 165237.

[31] XU Zhen, ZHAO Zhi-hao, WANG Gao-song, ZHANG Chao, CUI Jian-zhong. Microstructure and mechanical properties of the welding joint filled with microalloying 5183 aluminum welding wires [J]. International Journal of Minerals, Metallurgy, and Materials, 2014, 21: 577−581.

[32] HAN Kui, MAO Xie-min, OUYANG Zhi-ying, MIAO Chuan-rong, ZHANG Guang-quan. Behavior of rare earth elements in the degassing and purification process of cast aluminum melts [J]. Special Casting & Nonferrous Alloys, 2004(2): 61−62. (in Chinese)

[33] WANG Wei-du, PENG Shu-ming, LIANG Jian-hua, LONG Xing-gui, ZHOU Xiao-song. Isotope effect on thermodynamics of erbium dideuteride and ditritide [J]. Atomic Energy Science and Technology, 2013, 47: 1295−1299. (in Chinese)

[34] GIANOGLIO D, MAROLA S, BATTEZZATI L, AVERSA A, BOSIO F, LOMBARDI M, MANFREDI D, LORUSSO M. Banded microstructures in rapidly solidified Al−3wt.%Er [J]. Intermetallics, 2020, 119: 106724.

[35] LIU Guo-qiang. Influence mechanism of arc behaviors on molten pool flow and defect formation in tandem NG-GMAW of low alloy steel [D]. Shanghai: Shanghai Jiao Tong University, 2021. (in Chinese)

[36] NES E, RYUM N, HUNDERI O. On the Zener drag [J]. Acta Metallurgica, 1985, 33: 11−22.

[37] HU Ya-nan, WU Sheng-chuan, SHEN Zhao, CAO Hua-tang, ZHONG Xiang-li, WITHERS P J. Fine equiaxed zone induced softening and failure behavior of 7050 aluminum alloy hybrid laser welds [J]. Materials Science and Engineering: A, 2021, 821: 141597.

[38] HE Pei-dong, WEBSTER R F, YAKUBOV V, KONG Hui, YANG Qin, HUANG S, FERRY M, KRUZIC J J, LI Xiao-peng. Fatigue and dynamic aging behavior of a high strength

Al-5024 alloy fabricated by laser powder bed fusion additive manufacturing [J]. Acta Materialia, 2021, 220: 117312.

[39] HU Ya-nan, WU Sheng-chuan, GUO Yi, SHEN Zhao, KORSUNSKY A M, YU Yu-kuang, ZHANG Xu, FU Ya-nan, CHE Zhi-gang, XIAO Ti-qiao, LOZANO-PEREZ S, YUAN Qing-xi, ZHONG Xiang-li, ZENG Xiao-qin, KANG Guo-zheng, WITHERS P J. Inhibiting weld cracking in high-strength aluminum alloys [J]. Nature Communications, 2022, 13: 5816.

Er 对 Al−Mg−Er−Zr 合金双丝串列 GMAW 接头气孔及显微组织的影响

李嘉辉[1,2]，崔海超[1,2]，邵晨东[1,2]，兰 玲[1,2,3]，芦凤桂[1,2]

1. 上海交通大学 上海市激光制造与材料改性重点实验室，上海 200240；
2. 上海交通大学 材料科学与工程学院，上海 200240；
3. 中国船舶集团有限公司 上海船舶工艺研究所，上海 200032

摘 要：采用高效的双丝串列 GMAW 方法焊接一种新型 Al−Mg−Er−Zr 合金，并通过与 5083 铝合金焊接接头对比，研究 Er 对焊缝气孔率、接头显微组织和性能的影响。结果表明，Er 元素不仅能够降低熔池内游离氢的含量，使焊缝中的气孔率由 0.78%下降到 0.38%，还能够显著细化接头熔合区边界附近与焊缝金属的晶粒尺寸。熔合区边界附近的晶粒细化是由于母材中 $Al_3(Er,Zr)$粒子诱导发生了异质形核；焊缝晶粒尺寸的细化是由于焊缝中 Al_3Er 粒子发挥了钉扎晶界迁移的作用。添加 Er 后接头的极限抗拉强度由 272.44 MPa 提高到了 338.74 MPa，Al_3Er 的析出强化作用使接头强度提高了 20%。

关键词：Al−Mg−Er−Zr 合金；双丝串列 GMAW；气孔；显微组织；力学性能

(Edited by Xiang-qun LI)